Fast nuclear-spin conversion of H_2 trapped and polarized in a CO_2 matrix

Koichiro Yamakawa [*]

Advanced Science Research Center, Japan Atomic Energy Agency, Shirakata 2-4, Tokai, Naka, Ibaraki 319-1195, Japan

Atsuki Ishibashi,[†] Toshinobu Namiyoshi,[†] Yuichi Azuma, and Ichiro Arakawa
Department of Physics, Gakushuin University, 1-5-1 Mejiro, Toshima-ku, Tokyo 171-8588, Japan

The clear evidence for the nuclear spin conversion of matrix-isolated H_2 is presented. We trapped H_2 in a CO_2 film at 5.4 K and detected the induced infrared-absorption band including both the components of ortho and para H_2. By analyzing its time evolution, the conversion rate was determined to be 9.4×10^{-4} s^{-1}. We confirmed that this fast conversion was induced just by the CO_2 film with the uniquely unstable structure. We also identified H_2 at another kind of trapping sites, accompanied by higher anisotropy of the confining potential, and estimated its conversion rate to be 6×10^{-3} s^{-1}.

According to the resultant spin quantum number I of the two protons, H_2 exists in the nuclear spin isomers of ortho ($I = 1$) and para ($I = 0$). Because of the indistinguishablility of identical particles, each isomer couples to specific rotational states: ortho (para) H_2 takes only odd (even) values of the rotational quantum number J. The nuclear spin conversion (NSC) from ortho to para is strictly forbidden in the isolated state [1] but has been found to take place in condensed systems [2,3]. NSC studies have been promoted by a fundamental interest in its mechanism as well as industrial and astronomical demands [4].

While NSC on magnetic surfaces was interpreted in terms of the dipole interaction with inhomogeneous magnetic field [5], that on diamagnetic metal surfaces was described in the framework of the second perturbation theory, where the virtual electron transfer between a metal and H_2 is involved [6]. The conversion on the surfaces of diamagnetic insulators, such as metal-organic frameworks [7–9] and amorphous solid water (ASW) [10–14], has also been detected. The electric-field-induced conversion model was proposed as a possible candidate on the basis of the seventh-order perturbation theory [12]. On the other hand, Ilisca and Ghiglieno pointed out inseparability of the overlapped electron clouds of H_2 and an adsorbent, and alternatively developed the three-step conversion model [15–19] by extending the second-order perturbation mechanism described above [6].

The resonance-enhanced multiphoton ionization is a powerful and dominant technique for the NSC measurement of H_2 on surfaces [4] but cannot be directly applied to that inside solids because it needs to be combined with desorption techniques. On the other hand, the infrared absorption and Raman spectroscopy has an advantage of nondestructively detecting molecules. Indeed, NSC of polyatomic molecules such as H_2O [20,21] and CH_4 [22–26] in molecular solids has been intensively studied with the use of infrared spectroscopy. The conversion of matrix-isolated polyatomic molecules has been interpreted in terms of the quantum relaxation model [27,28], where the electron transfer between a trapped molecule and a matrix is not considered in contrast to the NSC models of H_2 [6,17]. For the purpose of comprehensively understanding the NSC mechanisms of diatomic and polyatomic molecules, their NSC rates measured in the same environment, i.e., the same matrix, are required to be compared [3]. In the present study, as the first step toward this purpose, we measured the induced infrared-absorption band of H_2 isolated in a CO_2 film as a function of time, and determined the NSC rate of H_2. This Rapid Communication provides solid evidence for NSC of matrix-isolated H_2.

The details of our experimental apparatus, which mainly consists of a Fourier transform infrared spectrometer, a sample chamber, and an external HgCdTe detector, were described elsewhere [20]. The pressure inside the chamber was measured with an extractor gauge and went down to 1×10^{-8} Pa after degassing at 393 K for 24 h. A gold substrate was cooled down to 5.4 K with a continuous liquid-helium flow cryostat, which was mounted on the chamber. The substrate temperature was measured with a silicon diode. A gas handling system was preliminarily evacuated by a turbo molecular pump and was degassed at 373 K for 24 h. The gases of CO_2 (99.99% purity) and H_2 (99.9995% purity) were mixed in the handling system, and the dilution D defined by the partial-pressure ratio of CO_2 to H_2 was set to be 100 with the use of a quartz oscillator gauge. The gas mixture was introduced into the sample chamber through an orifice at the end of a gas dosing tube directed toward the substrate and was condensed on the substrate at 5.4 K for 10 min. The flow rate was controlled by a variable leak valve such that the pressure in the chamber was kept at 4.0×10^{-3} Pa during the deposition.

---
[*]Corresponding author: yamakawa.koichiro@jaea.go.jp
[†]Present address: Institute of Low Temperature Science (ILTS), Hokkaido University, Sapporo 060-819, Japan.
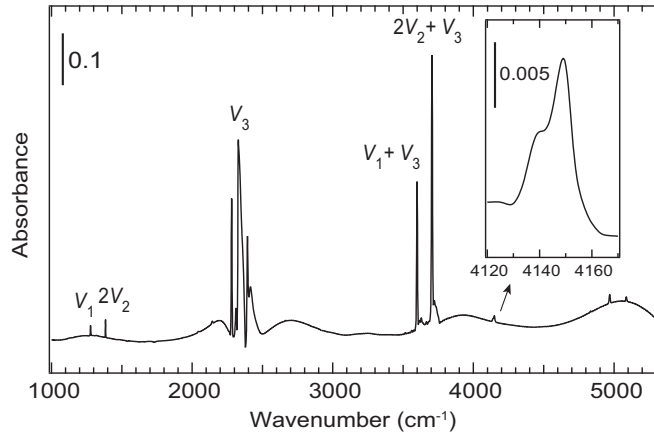
FIG. 1. Infrared-absorption spectrum of an H_2-containing CO_2 film deposited on the gold substrate at 5.4 K. The spectrum was measured just after the deposition with an accumulation number of 100. The symmetric stretching, bending, and antisymmetric stretching vibrations of CO_2 are denoted by ν_1, ν_2, and ν_3, respectively. The inset enlarges the induced absorption band of H_2.

Infrared absorption spectra were measured as a function of time in the reflection configuration after the deposition. The incident angle of the infrared light θ was $80°$, and the spectral resolution was 2 cm^{-1}.

Figure 1 shows the infrared spectrum of an H_2-containing CO_2 film just after the deposition. We define $t = 0$ s as the moment when this spectrum started to be recorded. The film interference resulted in the modulated baseline [29] as well as the distorted and suppressed ν_3-fundamental band of CO_2. The film thickness was evaluated to be 4.5 μm from the modulated baseline [30]. We confirmed the absence of absorption signals in the vicinity of 1590 cm^{-1}, where the most intense absorption band of matrix-isolated H_2O appears [31]; thus, the contamination of H_2O in the film was negligible. As shown in the inset of Fig. 1, we detected the induced infrared-absorption band of H_2 around 4150 cm^{-1}.

Figure 2 shows the time evolution of the H_2 band after $t = 240$ s as well as the results of fitting to Gaussian functions. The evolution before 240 s will be shown later. The spectrum at 3360 s in Fig. 2(b) has an asymmetric shape, so that it was not fitted to one Gaussian curve. Alternatively, it was well reproduced by two Gaussian curves centered at 4149 and 4147 cm^{-1}, which were labeled G_1 and G_2, respectively. The spectrum at 240 s in Fig. 2(a) was still not reproduced by these two components but successfully was upon adding another at 4138 cm^{-1}, labeled G_3. Note that the temporal changes in the optimized positions of G_1 and G_2 after 240 s were both within 0.6 cm^{-1} and that the integrated intensities of the G_2 curves at 240 and 3360 s differed only by 2%. Thus, we obtained the fitting result displayed in Fig. 2(a) by fixing the position, width, and height of G_2 at those in Fig. 2(b).

Whereas G_1 grew with time, G_3 decayed. With use of the tri-Gaussian fitting, we obtained the integrated intensities of G_1 and G_3 after 240 s as functions of time, which are displayed in Fig. 3. Since G_2 was almost time invariant as described above, it was fixed in a series of the tri-Gaussian fitting procedures. The integrated intensity of G_m ($m = 1, 3$)
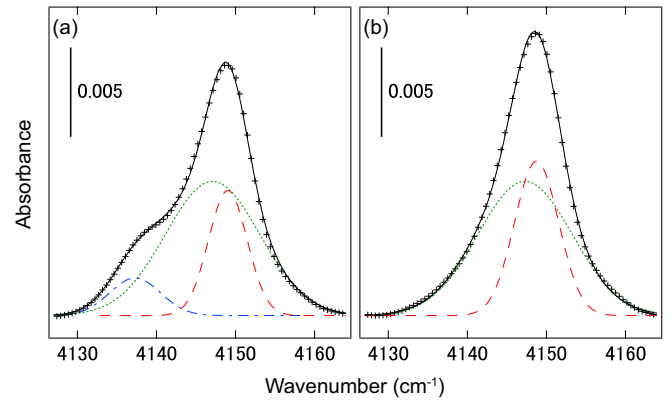

FIG. 2. Time development of the induced infrared-absorption band of H_2 trapped in solid CO_2 at 5.4 K: (a) $t = 240$ s and (b) $t = 3360$ s. The baselines were modified to be horizontal. The experimental data are denoted by crosses while the results of multi-Gaussian fitting by solid lines. The Gaussian functions of G_1, G_2, and G_3 are represented by dashed, dotted, and dashed-dotted lines, respectively.

was fitted to the following monoexponential function:

$$I_m(t) = [I_m(0) - I_m(\infty)] \exp(-k_m t) + I_m(\infty), \quad (1)$$

where k_m is the relaxation rate and $I_m(0)$ [$I_m(\infty)$] denotes the initial (equilibrium) integrated intensity. We obtained $k_1 = (9.6 \pm 0.4) \times 10^{-4}$ s^{-1} and $k_3 = (9.2 \pm 0.4) \times 10^{-4}$ s^{-1}. The inset of Fig. 3 is a schematic diagram of the transitions yielding G_1 and G_3. Since k_1 and k_3 coincided within the experimental error, the time evolution of the infrared spectrum was ascribed to the rotational relaxation of H_2 from $J = 1$ to $J = 0$ accompanied by the ortho-to-para conversion; as shown in the inset of Fig. 3, we attributed G_1 to $Q_1(0)$ of para H_2 and G_3 to $Q_1(1)$ of ortho H_2, where the subscript of Q indicates the
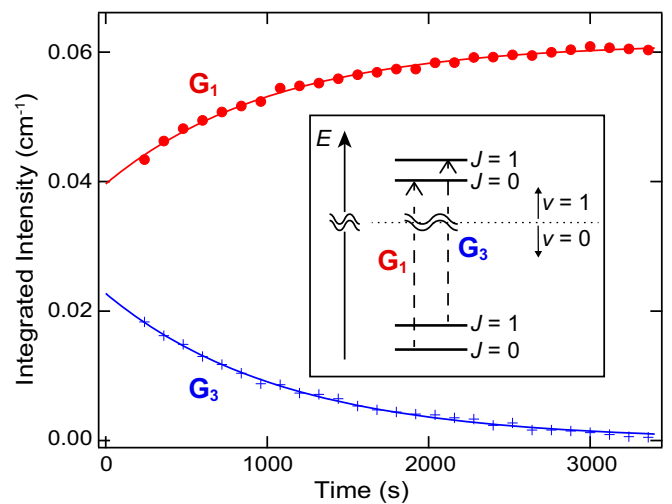

FIG. 3. Time-dependent integrated intensities of the absorption components of para H_2 (G_1, circles) and ortho H_2 (G_3, crosses) after $t = 240$ s. The results of monoexponential fitting are represented by solid lines. The inset schematically shows the transitions of G_1 and G_3. The quantum number of the stretching vibration is represented by v.

TABLE I. Frequencies of the $Q_1(0)$ and $Q_1(1)$ bands of H$_2$ in the gas and solid phases, inside matrices, and on surfaces. The magnitude of the frequency shift of $Q_1(0)$ from the gas-phase value is also shown. Raman (IR) means the data obtained by Raman (infrared-absorption) spectroscopy.

| | | | | Matrix | | | | Surface | |
| | | | | N$_2$ | | CO | | | |
	Gas[a]	Solid[b]	CO$_2$[c]	Raman[d]	IR[e]	Raman[d]	IR[e]	D$_2$O[f]	NaCl[g]
$Q_1(0)$	4161.1	4151.8	4149 (G_1)	4147.1	4144	4144.0	4144	4141	4133
$Q_1(1)$	4155.3	4143.4	4138 (G_3)	4139.9	4137	4136.1	4137	4132	4122
$|\Delta Q_1(0)|$		9.3	12	14.0	17	17.1	17	20	28

[a]Calculated from data in Ref. [36].
[b]Reference [37].
[c]This work. $T = 5.4$ K and $D = 100$.
[d]Reference [33]. $T = 15$ K and $D = 100$.
[e]Reference [31]. $T = 13$ K and $D = 5$–33.
[f]Reference [34]. $T = 12$ K.
[g]Reference [35]. $T = 30$ K.

increase of the stretching-vibrational quantum number [32]. The origin of G_2 will be discussed later.

In Table I, the frequencies of $Q_1(0)$ and $Q_1(1)$ are compared with those of H$_2$ inside other matrices [31,33], on surfaces [34,35], and in the gas [36] and solid [37] phases. The vibrational-frequency shift from the gas-phase value is represented by $\Delta Q_1(0)$. In the cavities of NaA zeolites, H$_2$ showed the vibrational-frequency shift of -87 cm^{-1}, from which the electric-field intensity was calculated to be on the order of 10^{10} V/m within the framework of the vibrational Stark effect [38]. However, because all of the $|\Delta Q_1(0)|$ values displayed in Table I, particularly those for matrices, are much smaller than 87 cm^{-1}, the Stark mechanism is not suitable for describing the frequency shift or polarization of H$_2$ at least in matrices. Indeed, the matrix-induced shift has been interpreted by explicitly considering the interaction potential between H$_2$ and a matrix molecule [39,40]. Once the equilibrium between the ortho and para species is achieved at 5.4 K, the ortho-to-para ratio (OPR) of H$_2$ almost equals zero [4]; OPR is as low as 10^{-14} in the free rotational state. Thus, the apparent absence of G_3 in the spectrum of Fig. 2(b) was reasonable. By the fitting to Eq. (1), we obtained $|[I_3(0) - I_3(\infty)]/[I_1(0) - I_1(\infty)]| = 1.0$, which means the band-strength ratio of $Q_1(1)$ to $Q_1(0)$. This result is totally consistent with the fact that band strength of $Q_1(J)$ does not depend on J [40].

Warren *et al.* observed the purely rotational bands of ortho and para H$_2$ in solid Ar and reported the 25% decrease of OPR after 2–3 days though neither the time evolution of the spectrum nor the NSC rate was provided [31]. Hixson *et al.* measured the temporal change in the induced infrared-absorption band of H$_2$ adsorbed on amorphous D$_2$O ice and roughly estimated the conversion half-life at 40 min [34]. In both of these studies, NSC of H$_2$ was ascribed to the accidental contamination of paramagnetic impurities. In our experiments, we carefully eliminated the contamination by preliminary degassing, which was not described in the literature of previous infrared- and Raman-spectroscopic studies [31,33,34,40,41]. The ultimate pressure of 1×10^{-8} Pa at room temperature indicated the negligible leak of air containing the NSC catalyst

of O$_2$. The contamination of H$_2$O was also negligible as described above. Thus, we conclude that NSC of H$_2$ was induced just by the CO$_2$ matrix.

Since the Stark effect is not the main cause of the matrix-induced vibrational shift, the electric-field-induced NSC mechanism [12] is not operative at least in the matrix-isolation systems. A possible candidate to describe NSC of H$_2$ in the CO$_2$ matrix is the three-step conversion model [17], where the Coulomb interaction causes the electron exchange between H$_2$ and the matrix in the first step, the hyperfine contact interaction brings about the simultaneous singlet-triplet transitions of the electronic and nuclear states of H$_2$ in the second, and the spin-orbit interaction finally realizes the electronic singlet-triplet transition inside the matrix. Ilisca applied this NSC model to H$_2$ adsorbed on ASW [19] and succeeded in reproducing the anomalous temperature dependence of the NSC rate in the range of 9.2–16 K [14]. It is notable that the rate of H$_2$ in solid CO$_2$ at 5.4 K is even faster than that on ASW at 9.2 K, 2×10^{-4} s^{-1}.

The CO$_2$ film deposited below $\sim$10 K is characterized by its porous and amorphous structure with the enhanced surface area and has a unique feature of randomly exhibiting abrupt rises of the substrate temperature named "thermal spikes" during its deposition [42,43]. The thermal spikes are caused by the structural rearrangement of the film, which decreases the porosity and releases detectable heat. The spikes were found to emerge also in the present study [44] but have never been reported in the cases of other molecular solids. Thus, the characteristically unstable and porous structure of the CO$_2$ film is possibly related to fast NSC of H$_2$.

We extrapolated the fitting curves in Fig. 3 and found that OPR took the room-temperature value of 3 at $t = -780$ s. Since the deposition time was as short as 600 s, this analysis indicates that NSC proceeded more efficiently just during the condensation. A probable cause for the enhanced conversion is the repeated collision between H$_2$ and CO$_2$, which is involved in the dissipation of their translational energies and condensation.

Figure 4 shows the induced absorption bands of H$_2$ at $t = 0$ and 120 s. In the same way as the spectra after 240 s, we
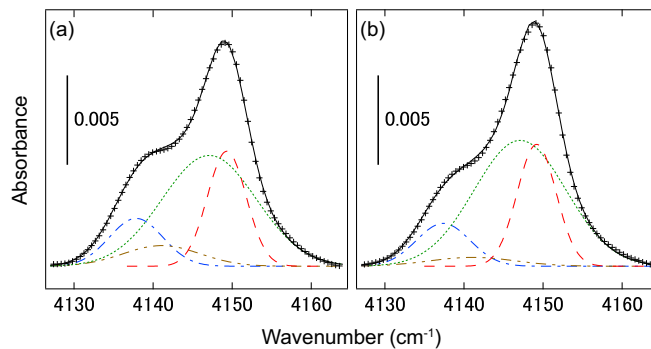
FIG. 4. The induced infrared-absorption bands of H_2 at (a) $t = 0$ s and (b) $t = 120$ s. The baselines were modified to be horizontal. The experimental data are represented by crosses while the results of tetra-Gaussian fitting by solid lines. The Gaussian functions of G_1, G_2, G_3, and G_4 are denoted by dashed, dotted, dashed-dotted, and dashed double-dotted lines, respectively.

first performed tri-Gaussian fitting by keeping G_2 fixed. The obtained integrated intensities of G_1 (G_3) were 0.032 (0.027) cm^{-1} at 0 s and 0.039 (0.022) cm^{-1} at 120 s, and were found to be significantly deviated from the monoexponential curves shown in Fig. 3. This means that to assume the invariance of G_2 before 240 s was not appropriate; in fact, without the fixation of G_2, its position at 0 s optimized by tri-Gaussian fitting was 4146 cm^{-1} rather than 4147 cm^{-1}. Therefore, we added another component G_4 to perform tetra-Gaussian fitting instead, as displayed in Fig. 4. Upon fitting, we fixed the position of G_2 at 4147 cm^{-1} and the integrated intensities of G_1 and G_3 at the values determined by the monoexponential curves in Fig. 3. Figure 4 shows the decay of G_4 at 4141 cm^{-1} as well as the growth of G_2 in the time range of 0–120 s. The integrated intensities of G_2 (G_4) were determined to be 0.093 (0.014) cm^{-1} at 0 s and 0.102 (0.007) cm^{-1} at 120 s while the integrated intensity of G_2 in Fig. 2 was 0.112 cm^{-1}.

The results described above show that the CO_2 film included two kinds of trapping sites for H_2: G_1 (G_3) was attributed to para (ortho) H_2 at site A and G_2 (G_4) to para (ortho) H_2 at site B. The NSC rate at site B was estimated from the

integrated-intensity changes of G_2 and G_4 to be 6×10^{-3} s^{-1}, which is about six times as high as that at site A. In addition, the frequency difference of G_2 and G_4, being about half as large as that of G_1 and G_3, suggests the approach of the lowest rotational levels of ortho and para H_2. Thus, we argue that the anisotropy of the confining potential at site B was higher than that at site A, and that the rotation of H_2 trapped at site B was more strongly hidered. Indeed, H_2 performing strongly hindered rotation on the surfaces of Cu(510) [45], and Pd(210) [46] was found to exhibit high-speed NSC at rates on the order of 1 s^{-1}. Regarding the polyatomic molecule of H_2O, it was also shown by calculation that the limitation on molecular rotation enhances mixing of the ortho and para rotational levels and therefore promotes NSC [47].

In summary, we measured the induced infrared-absorption band of H_2 in a CO_2 film at 5.4 K. Analyzing the time evolution, we found the band to consist of four components and the film to possess two kinds of trapping sites for H_2: G_1 at 4149 cm^{-1} (G_2 at 4147 cm^{-1}) and G_3 at 4138 cm^{-1} (G_4 at 4141 cm^{-1}) were assigned to $Q_1(0)$ of the para isomer and $Q_1(1)$ of the ortho isomer of H_2 at site A (B), respectively. Site B was characterized by the anisotropic confining potential compared with site A. The monoexponential growth of G_1 and decay of G_3 were ascribed to NSC of H_2 on the grounds that these components had the same relaxation rate and band strength. The NSC rate of H_2 at site A was determined to be 9.4×10^{-4} s^{-1}, which is even higher than that on ASW at 9.2 K. The negligible contamination indicated that fast NSC was induced just by the deposited film of CO_2, which has a uniquely unstable and porous structure. We also estimated the rate at site B to be as high as 6×10^{-3} s^{-1}. Our detection of NSC of matrix-isolated H_2 was allowed by the fast sample deposition, which should be also applied to other matrices in order to comprehensively understand the NSC mechanisms of diatomic and polyatomic molecules.

[1] K. Pachucki and J. Komasa, Phys. Rev. A **77**, 030501(R) (2008).

[2] E. Ilisca, Prog. Surf. Sci. **41**, 217 (1992).

[3] K. Yamakawa and K. Fukutani, J. Phys. Soc. Jpn. **89**, 051016 (2020).

[4] K. Fukutani and T. Sugimoto, Prog. Surf. Sci. **88**, 279 (2013).

[5] E. Wigner, Z. Phys. Chem. B **23**, 28 (1933).

[6] E. Ilisca, Phys. Rev. Lett. **66**, 667 (1991).

[7] S. A. FitzGerald, K. Allen, P. Landerman, J. Hopkins, J. Matters, R. Myers, and J. L. C. Rowsell, Phys. Rev. B **77**, 224301 (2008).

[8] S. A. FitzGerald, J. Hopkins, B. Burkholder, M. Friedman, and J. L. C. Rowsell, Phys. Rev. B **81**, 104305 (2010).

[9] S. A. FitzGerald, B. Burkholder, M. Friedman, J. B. Hopkins, C. J. Pierce, J. M. Schloss, B. Thompson, and J. L. C. Rowsell, J. Am. Chem. Soc. **133**, 20310 (2011).

[10] L. Amiaud, A. Momeni, F. Dulieu, J. H. Fillion, E. Matar, and J. L. Lemaire, Phys. Rev. Lett. **100**, 056101 (2008).

[11] N. Watanabe, Y. Kimura, A. Kouchi, T. Chigai, T. Hama, and V. Pirronello, Astrophys. J. Lett. **714**, L233 (2010).

[12] T. Sugimoto and K. Fukutani, Nat. Phys. **7**, 307 (2011).

[13] M. Chehrouri, J.-H. Fillion, H. Chaabouni, H. Mokrane, E. Congiu, F. Dulieu, E. Matar, X. Michaut, and J. Lemaire, Phys. Chem. Chem. Phys. **13**, 2172 (2011).

[14] H. Ueta, N. Watanabe, T. Hama, and A. Kouchi, Phys. Rev. Lett. **116**, 253201 (2016).

[15] E. Ilisca, Europhys. Lett. **104**, 18001 (2013).

[16] E. Ilisca and F. Ghiglieno, Eur. J. Phys. B **87**, 235 (2014).

[17] E. Ilisca and F. Ghiglieno, R. Soc. Open Sci. **3**, 160042 (2016).

[18] E. Ilisca and F. Ghiglieno, Chem. Phys. Lett. **667**, 233 (2017).

[19] E. Ilisca, Chem. Phys. Lett. **713**, 289 (2018).

[20] K. Yamakawa, S. Azami, and I. Arakawa, Eur. Phys. J. D **71**, 70 (2017).

[21] P. A. Turgeon, J. Vermette, G. Alexandrowicz, Y. Peperstraete, L. Philippe, M. Bertin, J. H. Fillion, X. Michaut, and P. Ayotte, J. Phys. Chem. A **121**, 1571 (2017).

[22] Y. Miyamoto, M. Fushitani, D. Ando, and T. Momose, J. Chem. Phys. **128**, 114502 (2008).

[23] A. Lekic, Ph.D. thesis, Université Pierre et Marie Curie-Paris 6, 2011.

[24] T. Sugimoto, I. Arakawa, and K. Yamakawa, Eur. Phys. J. D **72**, 42 (2018).

[25] T. Sugimoto, K. Yamakawa, and I. Arakawa, J. Chem. Phys. **143**, 224305 (2015).

[26] T. Sugimoto, H. Nasu, I. Arakawa, and K. Yamakawa, J. Chem. Phys. **150**, 184302 (2019).

[27] P. L. Chapovsky, Phys. Rev. A **43**, 3624 (1991).

[28] E. Ilisca and K. Bahloul, Phys. Rev. A **57**, 4296 (1998).

[29] N. J. Harrick, Appl. Opt. **10**, 2344 (1971).

[30] See Supplemental Material at http://link.aps.org/supplemental/10.1103/PhysRevB.102.041401 for the analytical method to obtain the film thickness.

[31] J. A. Warren, G. R. Smith, and W. A. Guillory, J. Chem. Phys. **72**, 4901 (1980).

[32] Strictly speaking, J is no longer a good quantum number but is still used for labeling the nearly-free-rotational levels. The slight anisotropy of the confining potential also resolves the rotational degeneracy of the $J = 1$ level; the lowest one among the split $J = 1$ levels is predominantly occupied at 5.4 K and is solely shown in the inset of Fig. 3.

[33] A. Kornath, A. Zoermer, and I. Köper, Spectrochim. Acta A **55**, 2593 (1999).

[34] H. G. Hixson, M. J. Wojcik, M. S. Devlin, J. P. Devlin, and V. Buch, J. Chem. Phys. **97**, 753 (1992).

[35] D. J. Dai and G. E. Ewing, J. Chem. Phys. **98**, 5050 (1993).

[36] I. Dabrowski, Can. J. Phys. **62**, 1639 (1984).

[37] S. S. Bhatnagar, E. J. Allin, and H. L. Welshy, Can. J. Phys. **40**, 9 (1962).

[38] N. Bras, J. Chem. Phys. **110**, 5943 (1999).

[39] V. Chandrasekharan, M. Chergui, B. Silvi, and R. D. Etters, J. Phys. Chem. **91**, 1623 (1987).

[40] M. E. Alikhani, B. Silvi, J. P. Perchard, and V. Chandrasekharan, J. Chem. Phys. **90**, 5221 (1989).

[41] F. T. Prochaska and L. Andrews, J. Chem. Phys. **67**, 1139 (1977).

[42] I. Arakawa, M. Kobayashi, and Y. Tuzi, J. Vac. Sci. Technol. **16**, 738 (1979).

[43] M. Falk, J. Chem. Phys. **86**, 560 (1987).

[44] See Supplemental Material at http://link.aps.org/supplemental/10.1103/PhysRevB.102.041401 for measured thermal spikes.

[45] K. Svensson and S. Andersson, Phys. Rev. Lett. **98**, 096105 (2007).

[46] S. Ohno, D. Ivanov, S. Ogura, M. Wilde, E. F. Arguelles, W. A. Diño, H. Kasai, and K. Fukutani, Phys. Rev. B **97**, 085436 (2018).

[47] H.-H. Limbach, G. Buntkowsky, J. Matthes, S. Gründemann, T. Pery, B. Walaszek, and B. Chaudret, Chem. Phys. Chem. **7**, 551 (2006).